FT-IR, FT-Raman, UV-Visible, and NMR spectroscopy and vibrational properties of the labdane-type diterpene 13-epi-sclareol

ARTICLE *in* SPECTROCHIMICA ACTA PART A MOLECULAR AND BIOMOLECULAR SPECTROSCOPY · NOVEMBER 2015

Impact Factor: 2.35 · DOI: 10.1016/j.saa.2014.11.049

5 AUTHORS, INCLUDING:

Fernando Chain
INSIBIO-CONICET
6 PUBLICATIONS **11** CITATIONS
SEE PROFILE

Patricio Leyton
Pontificia Universidad Católica de Valparaíso
39 PUBLICATIONS **540** CITATIONS
SEE PROFILE

Carolina Paipa
Pontificia Universidad Católica de Valparaíso
17 PUBLICATIONS **113** CITATIONS
SEE PROFILE

Silvia A Brandán
National University of Tucuman
123 PUBLICATIONS **897** CITATIONS
SEE PROFILE

Spectrochimica Acta Part A: Molecular and Biomolecular Spectroscopy 138 (2015) 303–313

Contents lists available at ScienceDirect

Spectrochimica Acta Part A: Molecular and Biomolecular Spectroscopy

journal homepage: www.elsevier.com/locate/saa

FT-IR, FT-Raman, UV–Visible, and NMR spectroscopy and vibrational properties of the labdane-type diterpene 13-*epi*-sclareol

Fernando E. Chain [a], Patricio Leyton [b], Carolina Paipa [c], Mario Fortuna [d], Silvia A. Brandán [e,*]

[a] *INQUINOA-CONICET, Instituto de Química Orgánica, Facultad de Bioquímica Química y Farmacia, Universidad Nacional de Tucumán, Ayacucho 471, 4000, San Miguel de Tucumán, Tucumán, Argentina*
[b] *Instituto de Química, Pontificia Universidad Católica de Valparaíso, Valparaíso, Chile*
[c] *Departamento de Ciencias Químicas, Facultad de Ciencias Exactas, Universidad Andrés Bello, Quillota 910, Viña del Mar, Chile*
[d] *Cátedra de Química Orgánica, Dpto. Cs. Básicas, Facultad de Agronomía y Zootecnia, Universidad Nacional de Tucumán, Av. Néstor Kirchner, 4000, San Miguel de Tucumán, Tucumán, Argentina*
[e] *Cátedra de Química General, Instituto de Química Inorgánica, Facultad de Bioquímica Química y Farmacia, Universidad Nacional de Tucumán, Ayacucho 471, 4000, San Miguel de Tucumán, Tucumán, Argentina*

HIGHLIGHTS

- FT-IR, FT-Raman, UV–Visible and NMR spectroscopies were used to study 13-*epi*-sclareol.
- Three stable structures for 13-*epi*-sclareol by DFT calculation were found.
- The ^{1}H NMR and ^{13}C NMR chemical shifts were predicted by DFT calculations.
- The complete vibrational assignment was performed for 13-*epi*-sclareol.
- The predicted UV–Vis spectrum demonstrates good correlation with the experimental one.

GRAPHICAL ABSTRACT

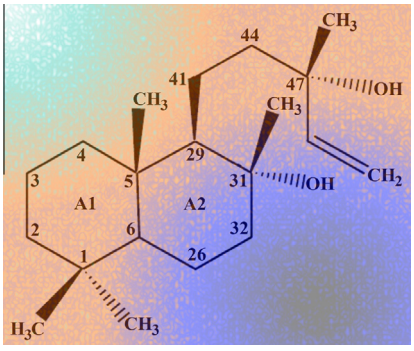

ARTICLE INFO

Article history:
Received 4 August 2014
Received in revised form 19 October 2014
Accepted 20 November 2014
Available online 29 November 2014

Keywords:
13-*epi*-sclareol
Vibrational spectra
Molecular structure
Force field
DFT calculations

ABSTRACT

In this work, FT-IR, FT-Raman, UV–Visible and NMR spectroscopies and density functional theory (DFT) calculations were employed to study the structural and vibrational properties of the labdane-type diterpene 13-*epi*-sclareol using the hybrid B3LYP method together with the 6-31G* basis set. Three stable structures with minimum energy found on the potential energy curves (PES) were optimized, and the corresponding molecular electrostatic potentials, atomic charges, bond orders, stabilization energies and topological properties were computed at the same approximation level. The complete assignment of the bands observed in the vibrational spectrum of 13-*epi*-sclareol was performed taking into account the internal symmetry coordinates for the three structures using the scaled quantum mechanical force field (SQMFF) methodology at the same level of theory. In addition, the force constants were calculated and compared with those reported in the literature for similar compounds. The predicted vibrational spectrum and the calculated ^{1}H NMR and ^{13}C NMR chemical shifts are in good agreement with the corresponding experimental results. The theoretical UV–Vis spectra for the most stable structure of 13-*epi*-sclareol demonstrate a better correlation with the corresponding experimental spectrum. The study of the three conformers by means of the theory of atoms in molecules (AIM) revealed different H bond interactions and a strong dependence of the interactions on the distance between the involved atoms. Furthermore, the natural bond orbital (NBO) calculations showed the characteristics of the electronic delocalization for the two six-membered rings with chair conformations.

* Corresponding author. Tel.: +54 381 4247752; fax: +54 381 4248169.
E-mail address: sbrandan@fbqf.unt.edu.ar (S.A. Brandán).

http://dx.doi.org/10.1016/j.saa.2014.11.049
1386-1425/

Introduction

Sesquiterpene derivatives, such as dehydrofukinone and cnicin, show several biological activities, including effects against diabetes, diarrhea, rheumatism, soreness and bacteria [1–8]. Recent investigations on the sesquiterpene lactone cnicin showed that it could act as a potential anti-tumor drug because it presents cytotoxic activity against multiple myeloma and strong anti-proliferative effects and induces death of primary myeloma cells even in the presence of survival cytokines in the tumor microenvironment [9]. Hence, in connection with its biological properties, studies on the structural and vibrational properties of these derivatives are of great chemical and pharmacological interest. Recently, the theoretical molecular structures of dehydrofukinone and cnicin were reported, and their corresponding vibrational spectra were completely assigned [10,11]. The presence of different OH and C=O groups in their structures predicted potential nucleophilic and electrophilic sites, which are associated with the regions reacting with potential biological compounds. In the present work, we studied the labdane-type diterpene 13-*epi*-sclareol (its IUPAC name is (1R,2R,4aS,8aS)-1-[(3S)-3-hydroxy-3-methyl-4-penten-1-yl]-2,5,8a-tetramethyldecahydro-2-naphthalenol). The biosynthesis of this compound in cell-free extracts from trichomas of *Nicotiana glutinosa* was reported by Guo and Wagner [12], its effect on fungal growth was studied by Bailey et al. [13], and its antimicrobial activity against four Gram-positive and three Gram-negative bacteria was tested by Mendoza et al. [14]. These authors have also studied the interaction of 13-*epi*-sclareol with the bacterial respiratory chain and have determined that the target site of 13-*epi*-sclareol is located between coenzyme Q and cytochrome c [15]. In a different study, Sashidhara et al. [16] isolated 13-*epi*-sclareol from *Coleus forskohlii*, a traditional herb in India, and demonstrated that the anti-proliferative activity of this lactone is comparable to that of Tamoxifen in terms of the IC_{50}; these researchers also showed concentration-dependent increased apoptotic changes in the breast cancer cell line MCF-7. An important study on the antibacterial activities of 15 terpenoids reported by Urzúa et al. [17] suggested that there are two structural requirements for these compounds to be active: a hydrophobic moiety consisting of a substituted decalin skeleton and a hydrophilic region possessing one hydrogen-bond donor group. These investigations showed that 13-*epi*-sclareol could act as a potential chemotherapeutic agent in tumor therapy, and its structural and vibrational properties should be studied for a complete characterization of this interesting substance. At present, its experimental structure has not been determined, and there are no theoretical studies related to its molecular electrostatic potentials, atomic charges, bond orders, stabilization energies and topological properties. Only the structure and absolute configuration of the derivative (−)-sclareol-8-acetate was reported by Bernardinelli et al. [18]. On the other hand, to characterize 13-*epi*-sclareol by means of vibrational spectroscopy, it is necessary to perform the complete assignment of the infrared and Raman spectra, which were unassigned until now. In this context, the goal of this work was to study the structural and vibrational properties of 13-*epi*-sclareol from the theoretical and experimental points of view through the combination of DFT calculations with vibrational spectra using the scaled quantum mechanical force field methodology (SQMFF) [19]. Thus, the initial structures of the compound, in accordance with those determined by Bernardinelli et al. [18] for (−)-sclareol-8-acetate, were first optimized, and the corresponding harmonic frequencies were then calculated using the hybrid B3LYP exchange correlation function with the 6-31G* basis set. Here, the complete assignment of the bands observed in the vibrational spectra of 13-*epi*-sclareol was performed taking into account the internal symmetry coordinates and the SQM force field at the same level of theory for the three structures considered. The force constants were also reported and compared with those published for dehydrofukinone and cnicin [10,11]. Moreover, the Merz–Kollman atomic charges [20], and the NBO [21,22], AIM [23,24] and HOMO–LUMO [25] calculations were used to compute the structural and topological properties and the energy gaps of the structures. In addition, the registered NMR and UV–Visible spectra were compared with the corresponding theoretical spectra, and good agreement was obtained between them. All the calculated structural and topological properties are carefully analyzed and discussed.

Experimental methods

General

The FT-IR spectra in the region of 4000–400 cm^{-1} were recorded on a Fourier Transform Infrared (FT-IR) Perkin Elmer Spectrum RX spectrometer equipped with a DTGS (Deuterated Tri-Glycerine Sulfate) detector. The spectral resolution was 2 cm^{-1}, and 16 scans were performed. The spectrum was measured by placing one drop of the pure sample between KBr windows. The Raman spectrum was recorded with a Renishaw Raman Microscope System RM2000 equipped with a diode laser providing a 634-nm line, a Leica microscope, an electrically cooled CCD (Charge Coupled Device) detector and a notch filter to eliminate elastic scattering. The spectrum was obtained using a 50× objective. The laser power output was 2.0 mW, and the spectral resolution was 2 cm^{-1}.

The Nuclear Magnetic Resonance (NMR) spectra were acquired on a Bruker Avance III instrument at 200 MHz (^1H) and 50 MHz (^{13}C) in $CDCl_3$, using the residual solvent as the integration standard. GC–MS analysis was performed on a Hewlett–Packard 6890 system with a Hewlett–Packard 5973 mass selective detector and a Perkin Elmer Elite-5MS column (5% phenyl-methyl siloxane, length 30 m × inner diameter 0.25 mm × film thickness 0.25 μm) with He as the carrier gas (1 mL min^{-1}; constant flow). The injector, GC–MS interphase, ion source and selective mass detector temperatures were maintained at 280, 280, 230 and 150 °C, respectively. The UV spectra were recorded on a Shimadzu 160 A UV–Vis spectrophotometer.

Plant material

Ixorhea tschudiana Fenzl was collected in January 2009 in Angastaco (1910 m.a.s.l.), Salta, Argentina. A voucher specimen was deposited in the herbarium of the Miguel Lillo Foundation (LIL. 597514). The material was positively identified as *I. tschudiana* Fenzl by Dr. Alberto Slanis.

Extraction and isolation of 13-epi-sclareol

The dried aerial parts (528 g) of *I. tschudiana* were extracted with CH_2Cl_2 (2 × 3 L) at rt for 36 h to yield 101 g of crude extract. The dried extract was then solubilized in EtOH at 60 °C, diluted with H_2O and extracted successively with n-hexane and CH_2Cl_2. Evaporation of the CH_2Cl_2 extracts at reduced pressure yielded 35.32 g. A portion (20 g) was subjected to column chromatography over Si gel (70–230 mesh) using CH_2Cl_2 followed by increasing concentrations of EtOAc (0–100%) to give 300 fractions, which were pooled based on TLC analysis [26].

Fraction 18 (0.5 g) gave white crystals, which were purified after repeated recrystallization from EtOH to afford pure 13-*epi*-sclareol (EPI, Fig. 1, mp 130–131 °C). The compound was

characterized by UV–Vis, IR, Raman, NMR and EI-MS spectroscopies, and its spectra were identical to those reported by Demetzo et al. [27] and Stierle et al. [28].

13-Epi-sclareol

Solid (colorless needles); UV (EtOH) λ_{max} 215 nm; IR ν 3329, 2956, 1475, 1386, 898 cm^{-1}; ^1H NMR ($CDCl_3$) δ 5.89 (1H, *dd*, *J* = 17, 11 Hz), 5.24 (1H, *dd*, *J* = 17, 1.5 Hz), 5.07 (1H, *dd*, *J* = 11, 1.5 Hz), 1.25 (3H, *s*), 1.14 (3H, *s*), 0.86 (3H, *s*), 0.78 (3H, *s*), 0.77 (3H, *s*). ^{13}C NMR ($CDCl_3$) δ_C 145.1 (*d*, C-54), 111.9 (*t*, C-55), 74.1 (*s*, C-47), 74.9 (*s*, C-31), 61.8 (*d*, C-29), 56.0 (*d*, C-6), 44.9 (*t*, C-32), 43.9 (*t*, C-44), 42.0 (*t*, C-2), 39.6 (*t*, C-4), 39.2 (*s*, C-5), 33.4 (*q*, C-18), 33.2 (*s*, C-1), 29.4 (*q*, C-50), 24.4 (*q*, C-35), 21.5 (*q*, C-14), 20.5 (*t*, C-41), 19.0 (*t*, C-26), 18.4 (*t*, C-3), 15.3 (*q*, C-22). MS *m/z* (rel. int.): 308 $[M]^+$ (5), 293 (10), 290 (20), 199 (80), 81 (90), 43 (100).

Computational details

The structure of EPI ($C_{20}H_{36}O_2$) has 58 atoms, and its initial geometry was modeled taking into account the reported structure for the (−)-sclareol-8-acetate derivative by Bernardinelli et al. [18] using the *GaussView* program [29]. In (−)-sclareol-8-acetate [17], the correct configuration of the C13 chiral center is 13R because the hydroxyl group is involved in an intermolecular hydrogen bond with the carbonyl oxygen of the acetate fragment. In EPI, the absence of the acetate group justifies the presence of other forms of EPI. In this work, in accordance with the potential energy surface, three structures were optimized at the B3LYP/6-31G* level of theory [30,31] using the Gaussian 09 package program [32]. The potential energy curves (PES) for the initial EPI structure described by the C29—C41—C44—C47, C41—C44—C47—C54, C41—C44—C47—C50, C44—C47—C54—C55 and C41—C44—C47—O48 dihedral angles were studied using the B3LYP/6-31G* level of theory. Hence, a total of nine configurations were founded on the PES of which only three have minimum energy and higher populations, as observed in Table S1 (Supporting Material). Then, the three configurations with minimum energy, named C1, C2 and C3, were considered in this work because, until now, the crystal and molecular structures of EPI are unknown. Fig. 1 shows a stereographic projection of EPI in which it is possible to observe the two six-membered rings fused in the chair configuration (A1 and A2), whereas in Fig. 2, the three stable structures of 13-*epi*-sclareol with C_1 symmetry and the labeling atoms are presented. Additionally, two charge types and bond orders were studied for the optimized

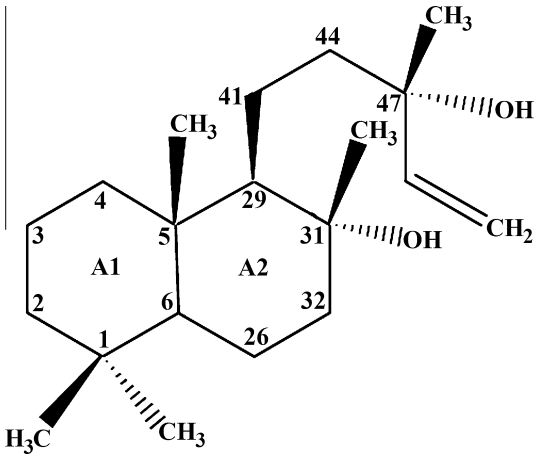

Fig. 1. Stereographic projection of the most stable structure of 13-*epi*-sclareol with the labeling atoms and the two rings of six members (A1 and A2).

EPI structures at the same theory level using the NBO calculation in the NBO 3.1 program [22] implemented in the Gaussian 09 package [32]. Two charge types were studied, namely natural population atomic (NPA) charges and those charges derived from Merz–Kollman [20]. The topological analysis of the three structures of EPI was performed using the AIM2000 program [24], whereas the harmonic force fields for the three configurations of the compound were computed with the MolVib program [33] at the B3LYP/6-31G* level using the SQMFF procedure [19]. The transformation of the resulting force fields to "natural" internal coordinates was performed by the MolVib program. Table S2 shows the natural internal coordinates for the three structures of EPI using definitions based on those reported for similar groups [10,11,34–46]. In general, potential energy distribution components (PED) ⩾ 10% were considered for the complete assignment using the resulting SQM. In some cases, such as those cases in which normal modes of vibrations are strongly mixed, potential energy distribution components (PED) between 10% and 5% were also considered. The nature of all of the normal modes of vibration was verified using the *GaussView* program [29]. For the three configurations of EPI, the calculated chemical shifts of the ^1H NMR and ^{13}C NMR spectra were obtained with the GIAO method [47] using the B3LYP/6-311++G** level of theory because better results are obtained at this theory level, as reported for other compounds [10,11,48–50]. Thus, the calculations were performed using TMS as a reference, whereas the UV–Vis spectra were predicted using TD-DFT calculations at the B3LYP/6-31G* level of theory with the Gaussian 09 program [32]. The structural, topological and vibrational properties for the three configurations were compared and analyzed.

Results and discussions

Geometry optimization

Table S3 shows the calculated total and relative energies and dipole moments for the more stable configuration of 13-*epi*-sclareol by using the B3LYP/6-31G* and B3LYP/6-31+G** methods. We observed that the most stable configuration C1 has a dipole moment value of 2.87 D by using the B3LYP/6-31G* method, whereas C2 is more stable than C3. The low energy differences between C1 and C2 and between C1 and C3 suggests that the three configurations could be present in the liquid sample because the high dipole moment value of C2 (3.67 D), in relation to C3, could in part justify its presence, as observed by us in various studies [37,49–52]. Besides, the proximity among the calculated relative energy values with the B3LYP/6-31+G** method support the presence of those three structures. The calculated bond lengths and dihedral angle parameters for C1, C2 and C3 obtained using the B3LYP/6-31G* method was compared with those experimental values determined for the (−)-sclareol-8-acetate derivative by Bernardinelli et al. [18] by means of X-ray diffraction. The calculated values are presented in Table S4, and the differences among these are expressed as the root-mean-square deviation (RMSD) values. The bond angles for the configurations were compared with the experimental values determined for the eremophilane sesquiternoid 6β,8β-dihydroxyeremophil-7(11)-en-8α, 12-olide using X-ray diffraction [53] because the bond angle values for (−)-sclareol-8-acetate have not been reported by Bernardinelli et al. [18]. The eremophilane sesquiternoid derivative possesses, similarly to EPI, two six-membered rings that adopt a chair configuration. A better correlation was observed using the B3LYP/6-31G* calculations for the bond lengths (between 0.0057 and 0053 Å), whereas the correlation ranges decrease for bond and dihedral angles to 1.07° and 23.2–4.1°, respectively. The differences observed can be attributed to the compared compound because

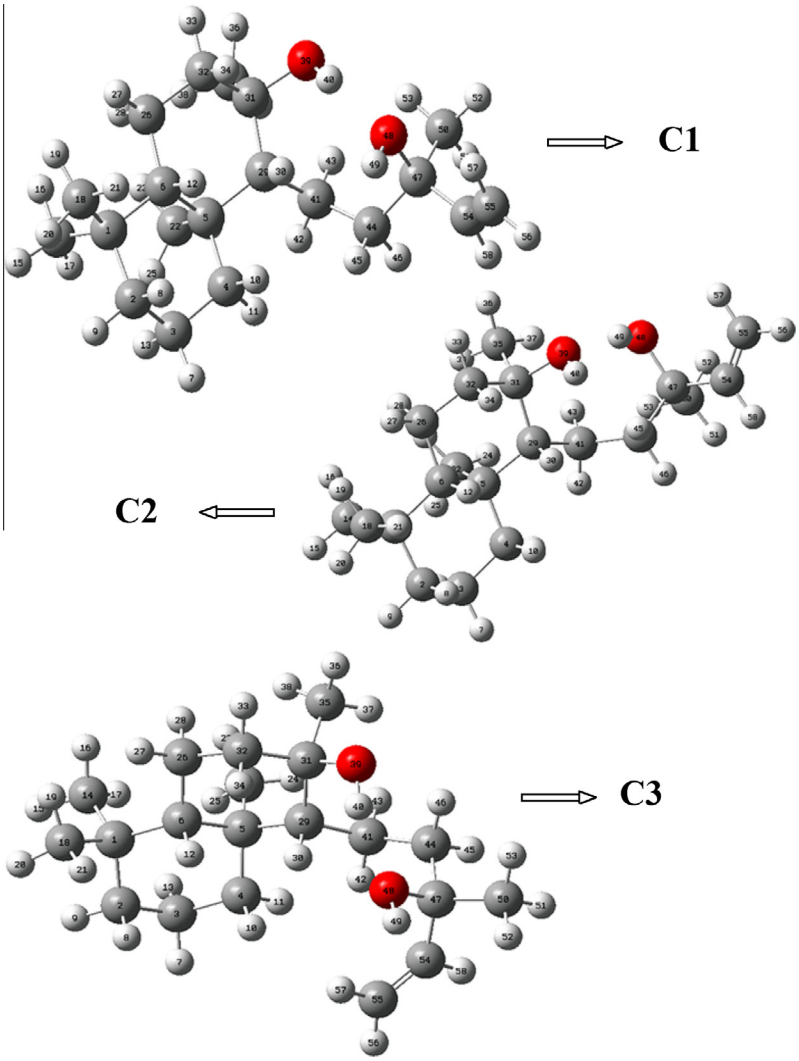

Fig. 2. Molecular structures corresponding to the C1, C2 and C3 conformers of 13-*epi*-sclareol and atoms numbering.

the hydroxyl group in (−)-sclareol-8-acetate is involved in an intermolecular hydrogen bond with the carbonyl oxygen of the acetate fragment. The C2 configuration of EPI has a lower RMSD value and exhibits a better correlation for the C29—C41—C44—C47 dihedral angle. In the three configurations of this compound, the double bonds belonging to the side chain, i.e., the C54═C55 bonds, are predicted to be larger than the experimental value of 1.243 Å, as observed in Table S4, whereas the C31—O39 and C47—O48 bonds are predicted to be shorter and larger, respectively, than the experimental values of 1.491 and 1.428 Å, respectively.

In accordance with the biological investigations performed on 13-*epi*-sclareol [16,54,55], there are two regions that are of importance for evaluating the compound as a potential chemotherapeutic agent in tumor therapy, a hydrophobic region and a hydrophilic region. For these structural requirements, it is necessary to analyze the distributions of charges on all the atoms of the three conformers of EPI and the corresponding electrostatic potentials. On the one hand, C1, the most stable configuration of EPI, has a dipole moment value of 2.87 D, as shown in Table S3, which is slightly lower than that of the sesquiterpene cnicin [11], whose dipole moment is 5.74 D because it has both OH and COO groups. In our case, the difference is justified because only two OH groups are present in the structures of the three configurations of EPI. On the other hand, the molecular electrostatic potential and two different charge types were analyzed for the C1, C2 and C3 configurations of EPI. The calculated molecular electrostatic potential values for the three configurations are summarized in Table S5. The surfaces, which are mapped only for the most stable configurations C1 and C2 are presented in Figs. S1 and S2, respectively. The molecular electrostatic potentials shows, as expected, that the higher negative values are located on the O39 and O48 atoms because these are the more electronegative atoms in EPI, as well as on the C atoms belonging to the CH_3 groups (C14, C18, C22, C35 and C50) and on the sp^2 C atoms of the double bond C54═C55. The values exhibit differences among the configurations having C1 and C3 the higher values, as observed in Table S5. Probably, the high values stabilize those configurations. On the other hand, the less negative values are observed on the H40 and H49 atoms belonging to the two OH groups. On the mapped surfaces of C1 and C2, a strong red color on the O atoms and a blue color on the H atoms are expected, as observed in Figs. S1 and S2, whereas the green color, observed on the remaining atoms, is associated with the hydrophobic regions. In summary, the red color is associated with the potential sites for the nucleophilic H bond formation, whereas the blue color is associated with potential electrophilic regions. In this work, for the three configurations of EPI, three charge types were calculated using the 6-31G* basis set, namely Mulliken charges, natural atomic charges (NPA) and

Merz–Kollman (MK) charges [20]; the corresponding values are given in Table S6. The analysis of these values revealed that the three charges exhibit differences for all the atoms, with the Merz–Kollman charges on the O atoms having similar values to the Mulliken charges but slightly different values from the NPA charges. The highly negative atomic charge values are located on the O39 and O48 atoms of the three configurations of EPI, whereas the highly positive atomic charge values are observed on the H40 and H49 atoms belonging to the OH groups. A very important difference between both charges is observed on the C54 atoms of the three configurations because the MK and NPA charges are higher than the Mulliken charges. This analysis shows significant differences among the three configurations, where C1 and C3 are the most stable configurations due to the higher charge distributions on the O and H atoms of both OH groups and the lower charges on the C atoms associated with the C=C bonds. On the contrary, possibly C2 is stable due to the lower charges on the C atoms associated with the C=C bonds.

NBO study

Due to the structural requirements necessary to present biological activity, the structural stabilities of the three configurations of EPI were also studied by employing bond orders, which are expressed as Wiberg indexes, and the second-order perturbation energies by means of NBO calculations [22] using the 6-31G* basis set. The bond order values are given in Table S7, and the results show that the C1 and C5 atoms have higher bond order values, as expected because they have sp^3 hybridization and are linked to four other C atoms, whereas the remaining C atoms are linked to C and H atoms. Furthermore, both the C54 and C55 atoms with sp^2 hybridization have high bond order values, as observed in Table S7, but the value is lower than that found for the C1 and C5 atoms.

The second-order perturbation energies $E^{(2)}$ (donor → acceptor) related to the most important delocalizations were studied for the three configurations of EPI at the B3LYP/6-31G* level of theory, and the results are presented in Table S8. For the three configurations, two contribution types of the stabilization energies were found, which are related to the skeletal part of EPI and to the lone pairs of oxygen atoms. These contributions are the $\Delta ET_{\sigma\rightarrow\sigma*}$ and $\Delta ET_{LP\rightarrow\sigma*}$ charge transfers, of which the former is the most important. In this compound, the total energy contribution is due principally to the skeletal part of EPI, in opposition to that observed in the sesquiterpene cnicin, where the lone pairs of the oxygen atoms ($\Delta ET_{LP\rightarrow\sigma*}$) and their high stability are associated with the presence of OH groups, a COO group and a lactone ring [11]. This analysis shows that the three configurations could be present in the liquid phase because the total energies of the C1 and C3 configurations are higher than the corresponding C2, partially supporting their presence.

AIM analysis

The stabilities of the C1, C2 and C3 configurations of EPI and the different electrostatic interactions were also studied using Bader's atoms in molecules theory [23] and the AIM2000 software [24]. Thus, the calculated topological properties, such as the electron charge density (ρ) and the *Laplacian* values $\nabla^2\rho(r)$ in the bond critical points (BCPs) can be observed in Table S9. The principal characteristics of these BCPs are that the $\rho(r)$ values should be between 0.05 and 0.3 a.u., the relationship $|\lambda 1|/\lambda 3$ should be < 1 and $\nabla^2\rho(r)$ should be positive with values between 0.04 and 0.2 a.u. These results indicate that the interaction is dominated by the contraction of charge away from the interatomic surface toward each nucleus [36–38,44–46]. The analysis shows clear differences among the three configurations, as observed in Table S9. For C1, there are twelve BCPs as H bonds interactions, nine of which are H---H bonds and three of which are O---H interactions, as observed in Table S9 and Fig. S3. For C2, nine BCPs are also observed, six of which are H---H bonds and three of which are O---H interactions. For C3, there are eleven BCPs as H bonds interactions where eight are H---H interactions, two are O---H interactions and, the remaining is a C---H interaction. For C1 and C3, the observed topological properties of the O48---H40 interactions have higher values than the other ones because the distances between the involved atoms are lower (1.937 and 1.930 Å, respectively) while for C2, the topological properties of the O39---H49 interactions have higher values than the other ones. A similar dependence on the distance is observed for the H11---H42 interactions of C2 and C3, where the properties have higher values due to the lower distances between the H11 and H42 atoms (1.958 and 1.994 Å, respectively) while for C3, the H24---H42 interaction present higher values with a distance between atoms of 2.087 Å, as observed in Table S9. These results clearly reveal (i) the high stability of C1 in relation to C2 and C3 due to the different nature of the H bonds formed, (ii) the high stabilities of C2 and C3 due to their numerous interactions that support the presence of both configurations in the liquid state, (iii) the strong dependence of the interactions on the distance between the involved atoms, and (iv) the strong dependence of the topological properties of the BCPs on the nature of the interactions than on the distances between the involved atoms because two different H bond interactions are observed in C1 and C2 while three H bond types are found in C3. Similar results were observed for the sesquiterpene cnicin [11].

NMR analysis

Tables S10 and S11 show a comparison between the chemical shifts calculated using the GIAO method for the ^{1}H and ^{13}C nuclei [47] with the corresponding experimental results, whereas the corresponding ^{1}H and ^{13}C NMR spectra for 13-*epi*-sclareol are presented in Figs. S4 and S5. Strong correlations are observed between the theoretical values and the corresponding experimental values for both the ^{1}H and ^{13}C nuclei, with RMSD values between 0.11 and 0.09 ppm for the ^{1}H nuclei and between 1.01 and 1.12 ppm for the ^{13}C nuclei. In general, the calculated shifts for the ^{13}C nuclei are higher than the corresponding experimental values, which is a different result from those observed for similar compounds [44,45]. The difference observed for some ^{1}H nuclei, such as H11, H13, H17, H23, H24, H25, H27, H38 and H43, can be attributed to the intra-molecular H bonds, as described in the above section. Some H atoms belonging to the CH_3 and CH_2 groups of the three configurations of EPI are involved in H bond interactions, as was revealed by AIM analysis; because of this, theoretical calculations do not correctly predict the ^{1}H chemical shifts for those groups (Table S10). This was also observed for dehydrofukinone [10]. For the three configurations of EPI, the theoretical calculations did not predict the chemical shifts for the H40 and H49 nuclei belonging to the OH groups (Table S10), probably because those atoms are involved in intra-molecular H bonds. Here, only the O39---H53, O48---H30 and O48---H40 interactions for the C1 configuration were predicted by the AIM calculations. Note the very good correlation between the experimental and calculated values for the ^{13}C nuclei of the three configurations of EPI and, especially the high value of the C55 atom corresponding to the C3 configuration. Probably, this value explains the C---H interaction in C3.

Vibrational analysis

In this analysis, we considered the three structures of EPI in accordance with the above calculation results. The three structures have C_1 symmetries and 168 normal vibration modes, all of which are active in the infrared and Raman spectra. A comparison between the recorded infrared and Raman spectra of the pure sample at room temperature can be observed in Fig. 3, and the comparisons between the experimental infrared and Raman spectra for the compound with the corresponding theoretical values calculated using the 6-31G* basis set are given in Figs. S6 and S7, respectively. In general, in the higher wavenumbers region, the theoretical IR spectra for C1, C2 and C3 present good concordances with the corresponding experimental spectra (Fig. S6), and the strong band predicted by SQM calculations at 3468 cm^{-1} for C1, which is assigned to an OH stretching mode, justifies the experimental broad band centered on 3329 cm^{-1} (Tables 1 and S12). Another very important observation is that the calculated IR spectra for C3 do not predict intense bands for both OH stretching modes, but on the contrary, the bands associated with those stretching modes in the corresponding Raman spectra are predicted with higher intensities, as observed in Tables S13 and S14 and Fig. S7. However, in the 4000–2800 cm^{-1} and 1900–1400 cm^{-1} regions in the theoretical Raman spectra for C1, C2 and C3, a good concordance with the corresponding experimental spectra is observed (Fig. S7). The complete assignment of the experimental bands to the normal modes of vibration of EPI was performed using the B3LYP/6-31G* approximation level and taking into account the PED contributions calculated through the SQMFF methodology [19] using the MolVib program [33]. It is necessary to clarify that scale factors [19] defined for the 6-31G* basis set was employed, and for this reason, this calculation level was used to determine the force fields of the three configurations of EPI. The assignments for the expected normal vibration modes of EPI, together with the corresponding experimental and SQM calculated wavenumbers based on the B3LYP/6-31G* calculations, are summarized in Table 1. The corresponding potential energy distributions and assignments for the C1, C2 and C3 configurations of EPI can be observed in Tables S12, S13 and S14, respectively. These tables show that the SQM contributions for the vibration modes number 166 of C1 and C2 and, the vibration mode number 167 for C3 were not predicted by calculations but rather assigned with the aid of the *GaussView* program [29]. These modes were identified by their characteristics, as indicated in Tables 1, S12, S13 and S14. Below, we discuss the assignment of some groups.

Band assignments

OH modes. For the three configurations of EPI, these modes are predicted by the SQM calculations as pure modes and thus can be easily assigned to the IR bands at 3329 and 3226 cm^{-1}. In agreement with the results obtained by AIM analysis and with the reported data for compounds containing OH groups [10,11,34,36–39,44,45,48,49,56], the form and broad of both IR bands indicate the presence of H bond interactions in the liquid phase. As predicted by the calculations, the corresponding deformation modes were assigned to the IR and Raman bands at 1242, 1083, 1136, 1411 and 1117 cm^{-1}, whereas the shoulder and Raman band at 339 and 329 cm^{-1}, respectively, were assigned to torsion modes of this group, as observed in Table 1.

CH modes. For the three configurations of EPI, only three CH stretching modes are expected, and these are associated with the C6—H12, C29—H30 and C54—H58 bonds. Theoretically, the two first modes are predicted in the 2851–2833 cm^{-1} region, whereas the remaining modes are predicted at higher wavenumbers in the 3026 and 3005 cm^{-1} region because they are associated with the —HC═C< moiety, as indicated in Table 1. Thus, they were assigned accordingly. The CH in-plane and out-of-plane deformation modes were assigned as the theoretical calculations predicted

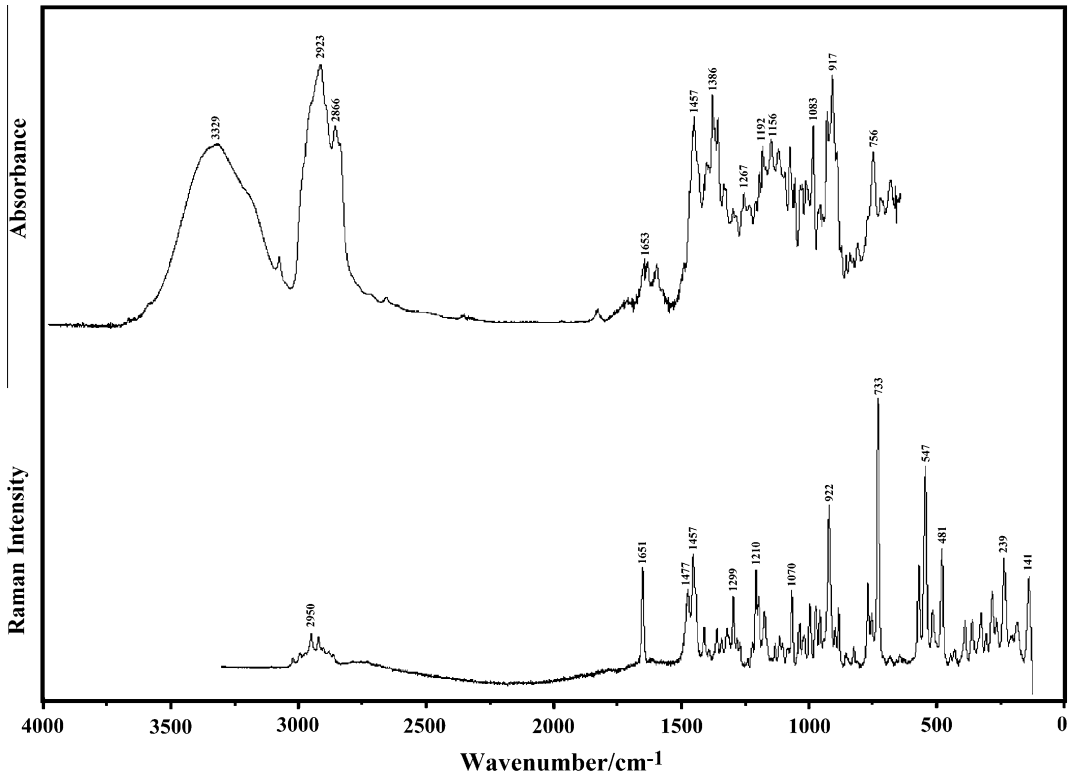

Fig. 3. Experimental infrared (upper) and Raman (bottom) spectra of 13-*epi*-sclareol.

Table 1
Observed and calculated wavenumbers (cm^{-1}) and assignment for 13-*epi*-sclareol.

Modes	Experimental		C1		C2		C3	
	IR[a]	Raman[a]	SQM[b]	Assignment[a]	SQM[b]	Assignment[a]	SQM[b]	Assignment[a]
1	3329 s,br		3567	ν(O48–H49)	3574	ν(O39–H40)	3575	ν(O48–H49)
2	3226 sh		3468	ν(O39–H40)	3437	ν(O48–H49)	3504	ν(O39–H40)
3	3084 w	3107 vw	3113	ν_aCH_2(C55)	3116	ν_aCH_2(C55)	3114	ν_aCH_2(C55)
4		3051 vw	3040	ν_sCH_2(C55)	3050	$\nu_{as}CH_3$(C35)	3040	ν_sCH_2(C55)
5		3042 vw	3034	$\nu_{as}CH_3$(C35)	3038	ν_sCH_2(C55)	3033	$\nu_{as}CH_3$(C35)
6		3022 w	3025	$\nu_{as}CH_3$(C50)	3023	$\nu_{as}CH_3$(C14)	3025	$\nu_{as}CH_3$(C14)
7		3022 w	3023	ν(C54–H58)	3018	$\nu_{as}CH_3$(C35)	3019	ν(C54–H58)
8			3022	$\nu_{as}CH_3$(C14)	3012	$\nu_{as}CH_3$(C22)	3014	$\nu_{as}CH_3$(C22)
9		3008 sh	3018	$\nu_{as}CH_3$(C22)	3008	$\nu_{as}CH_3$(C50)	3008	ν_aCH_2(C41)
10			3008	$\nu_{as}CH_3$(C50)	3005	ν(C54–H58)	3003	$\nu_{as}CH_3$(C22)
11			3002	$\nu_{as}CH_3$(C35)	3004	ν_aCH_2(C41)	3002	$\nu_{as}CH_3$(C50)
12			2999	$\nu_{as}CH_3$(C22)	3003	$\nu_{as}CH_3$(C22)	3001	$\nu_{as}CH_3$(C35)
13		2995 w	2990	$\nu_{as}CH_3$(C18)	2994	$\nu_{as}CH_3$(C50)	2990	$\nu_{as}CH_3$(C18)
14			2989	ν_aCH_2(C41)	2990	$\nu_{as}CH_3$(C18)	2982	ν_aCH_2(C41)
15			2978	$\nu_{as}CH_3$(C14)	2979	$\nu_{as}CH_3$(C14)	2982	$\nu_{as}CH_3$(C50)
16			2972	$\nu_{as}CH_3$(C18)	2977	ν_sCH_2(C41)	2976	$\nu_{as}CH_3$(C14)
17			2967	ν_aCH_2(C26)	2974	$\nu_{as}CH_3$(C18)	2972	$\nu_{as}CH_3$(C18)
18			2956	ν_aCH_2(C4)	2971	ν_aCH_2(C26)	2963	ν_aCH_2(C26)
19	2956 sh		2950	ν_aCH_2(C32)	2958	ν_aCH_2(C4)	2957	ν_aCH_2(C4)
20		2950 w	2948	ν_sCH_3(C22)	2956	ν_aCH_2(C32)	2951	ν_sCH_3(C22)
21			2946	ν_aCH_2(C3)	2953	ν_aCH_2(C41)	2948	ν_aCH_2(C32)
22			2943	ν_sCH_3(C35)	2949	ν_sCH_3(C22)	2944	ν_sCH_3(C35)
23			2942	ν_sCH_2(C41)	2948	ν_sCH_3(C35)	2943	ν_aCH_2(C3)
24			2939	ν_sCH_3(C50)	2947	ν_aCH_2(C3)	2934	ν_sCH_2(C41)
25			2931	ν_aCH_2(C41)	2934	ν_sCH_2(C26)	2930	ν_sCH_2(C26)
26			2930	ν_aCH_2(C2)	2932	ν_aCH_2(C2)	2927	ν_aCH_2(C2)
27		2922 w	2927	ν_sCH_2(C26)	2929	ν_sCH_3(C50)	2923	ν_sCH_3(C14)
28	2923 vs	2922 w	2924	ν_sCH_3(C14)	2926	ν_sCH_3(C14)	2919	ν_sCH_3(C50)
29			2914	ν_sCH_3(C18)	2919	ν_sCH_2(C41)	2917	ν_sC–H
30			2914	ν_aC–H	2915	ν_sCH_2(C3)	2914	ν_sCH_3(C18)
31	2901 sh	2902 vw	2904	ν_sCH_2(C41)	2914	ν_sCH_3(C18)	2912	ν_sCH_2(C3)
32			2901	ν_sCH_2(C32)	2893	ν_sCH_2(C4)	2910	ν_sCH_2(C41)
33		2879 vw	2894	ν_sC–H	2890	ν_sCH_2(C2)	2901	ν_sCH_2(C32)
34	2866 s	2863 vw	2888	ν_sCH_2(C4)	2880	ν_sCH_2(C32)	2900	ν_sCH_2(C4)
35	2847 sh	2844 vw	2886	ν_sCH_2(C2)	2851	ν_sC–H	2887	ν_sCH_2(C2)
36			2839	ν_aC–H	2839	ν_aC–H	2848	ν_aC–H
37	1653 w	1651 m	1657	ν(C54–C55)	1660	ν(C54–C55)	1659	ν(C54–C55)
38	1491 sh	1477 m	1491	$\delta_{as}CH_3$(C22)	1492	$\delta_{as}CH_3$(C35)	1490	$\delta_{as}CH_3$(C22)
39			1486	$\delta_{as}CH_3$(C22)	1485	$\delta_{as}CH_3$(C14)	1484	$\delta_{as}CH_3$(C14)
40	1475 sh		1479	$\delta_{as}CH_3$(C50)	1484	$\delta_{as}CH_3$(C22)	1476	$\delta_{as}CH_3$(C14)
41		1471 sh	1478	$\delta_{as}CH_3$(C18)	1474	$\delta_{as}CH_3$(C18)	1474	$\delta_{as}CH_3$(C18)
42	1469 sh		1475	$\delta_{as}CH_3$(C18)	1471	$\delta_{as}CH_3$(C22)	1469	$\delta_{as}CH_3$(C35)
43			1469	$\delta_{as}CH_3$(C14)	1469	$\delta_{as}CH_3$(C14)	1468	δCH_2(C26)
44			1467	$\delta_{as}CH_3$(C35)	1466	δCH_2(C41)	1464	δCH_2(C3)
45	1461 sh	1462 sh	1463	δCH_2(C4)	1464	$\delta_{as}CH_3$(C50)	1463	$\delta_{as}CH_3$(C50), ρCH_3(C50)
46			1459	$\delta_{as}CH_3$(C50)	1462	δCH_2(C3)	1456	$\delta_{as}CH_3$(C50)
47	1457 s	1457 vs	1457	δCH_2(C26)	1456	δCH_2(C44)	1455	$\delta_{as}CH_3$(C35)
48			1455	$\delta_{as}CH_3$(C35)	1455	δCH_2(C32), $\delta_{as}CH_3$(C22)	1454	$\delta_{as}CH_3$(C22)
49			1452	$\delta_{as}CH_3$(C14)	1451	δCH_2(C32), δCH_2(C26)	1451	$\delta_{as}CH_3$(C18)
50			1451	δCH_2(C41)	1450	$\delta_{as}CH_3$(C50)	1449	δCH_2(C32)
51		1447 sh	1449	δCH_2(C32)	1450	$\delta_{as}CH_3$(C18)	1447	δCH_2(C4)
52	1445 sh		1447	δCH_2(C3)	1447	δCH_2(C4)	1444	δCH_2(C2)
53			1442	δCH_2(C2)	1445	$\delta_{as}CH_3$(C35)	1441	δCH_2(C41)
54	1440 sh	1432 sh	1440	δCH_2(C44)	1442	δCH_2(C2)	1439	δCH_2(C44)
55		1411 w	1421	δ(O39–H40)	1405	δ(O48–H49)	1417	δ(O39–H40)
56	1409 w	1406 sh	1403	δCH_2(C55)	1401	δ_sCH_3(C35)	1405	δCH_2(C55)
57			1400	δ_sCH_3(C22)	1397	δ_sCH_3(C22)	1404	$wagCH_2$(C41)
58		1395 w	1398	δ_sCH_3(C14)	1396	δ_sCH_3(C14)	1395	δ_sCH_3(C22)
59	1386 s	1387 vw	1392	$wagCH_2$(C41)	1392	δCH_2(C55), ν(C47–C54)	1394	δ_sCH_3(C14)
60			1385	$wagCH_2$(C44)	1388	$wagCH_2$(C41)	1393	$wagCH_2$(C44)
61	1379 sh	1379 vw	1382	$wagCH_2$(C26)	1384	$wagCH_2$(C26)	1383	$wagCH_2$(C26)
62		1373 sh	1376	$wagCH_2$(C3)	1378	$wagCH_2$(C3)	1377	$wagCH_2$(C3)
63	1367 s		1369	δ_sCH_3(C18)	1369	δ_sCH_3(C50)	1369	$wagCH_2$(C2)
64	1367 s	1363 vw	1369	δ_sCH_3(C50)	1367	$wagCH_2$(C2)	1368	δ_sCH_3(C18)
65			1366	$wagCH_2$(C2)	1366	δ_sCH_3(C18)	1366	δ_sCH_3(C50)
66	1363 sh	1363 vw	1364	δ_sCH_3(C35)	1364	$wagCH_2$(C4)	1365	$wagCH_2$(C4)
67			1362	$wagCH_2$(C4)	1362	$wagCH_2$(C32)	1360	$wagCH_2$(C32)
68		1354 vw	1358	$wagCH_2$(C32)	1356	ρ′C29H30	1357	δ_sCH_3(C35)
69	1342 w	1343 w	1350	ρC6H12	1351	ρC6H12	1354	ρ′C29H30
70	1332 sh		1338	ρ′C29H30	1340	$wagCH_2$(C44)	1338	ρC6H12
71		1322 w	1330	δC47C54C55	1332	δC47C54C55	1330	δC47C54C55
72		1316 sh	1321	ρC29H30	1316	ρC29H30	1318	δ(O48–H49)
73	1304 w	1299 m	1310	δ(O48–H49)	1300	ρCH_2(C4)	1309	ρC29H30

(*continued on next page*)

Table 1 (*continued*)

Modes	Experimental		C1		C2		C3	
	IR[a]	Raman[a]	SQM[b]	Assignment[a]	SQM[b]	Assignment[a]	SQM[b]	Assignment[a]
74			1302	ρCH_2(C2)	1297	ρC54H58	1304	ρCH_2 (C4)
75	1293 sh		1295	ρC54H58	1293	ρCH_2(C2)	1296	ρCH_2(C2)
76		1285 w	1283	ρCH_2(C41)	1263	ρCH_2(C44)	1281	ρC54H58
77	1267 w	1271 w	1260	ρCH_2(C4)	1254	ρCH_2(C32)	1270	ρCH_2(C41)
78		1256 w	1247	ρCH_2(C32)	1252	ρCH_2(C44), ρC29H30	1250	ρCH_2(C41), ρC29H30
79	1242 w	1242 w	1226	ρCH_2(C44)	1232	ρCH_2(C41)	1243	ρCH_2(C32)
80	1219 w	1224 w	1221	ρCH_2(C26)	1222	ρCH_3(C18)	1220	ν(C1–C2)
81	1203 m	1210 s	1202	ρCH_2(C3)	1204	ρCH_2(C3)	1204	ρCH_2(C3)
82	1192 s	1199 m	1196	ν(C32–C31)	1197	ρCH_2(C26), ν(C32–C31)	1192	ν(C32–C31)
83	1186 sh		1188	ρCH_3(C14)	1184	ρCH_3(C14)	1189	ρCH_2(C26)
84	1186 sh		1181	ρCH_3(C22), ν(C4–C5)	1182	ρCH_3(C22)	1184	ρCH_3(C14)
85	1174 m	1177 m	1174	ρCH_3(C50)	1172	τR_1(A1)	1164	τR_1(A2)
86	1156 s	1165 sh	1162	$\rho' CH_3$(C22)	1158	ρCH_3(C35)	1159	βR_1(A1), τR_1(A1)
87	1128 s	1136 w	1159	ρCH_3(C50), ν(C44–C47)	1149	ν(C44–C47)	1153	ρCH_2(C44)
88	1119 sh	1117 m	1148	$\rho' CH_3$(C50)	1141	ρCH_3(C50)	1124	$\rho' CH_3$(C35)
89	1103 m	1106 w	1125	ν(C29–C31)	1112	$\rho' CH_3$(C22)	1116	ρCH_3(C35)
90	1083 s	1087 vw	1108	$\rho' CH_3$(C22)	1104	δ(O39–H40)	1105	$\rho' CH_3$(C22)
91		1070 s	1078	ν(C6–C26)	1079	ν(C47–C50)	1079	ν(C44–C47)
92	1063 m		1064	ν(C29–C41), ν(C47–C50)	1068	ν(C6–C26)	1074	ν(C6–C26)
93			1054	ν(C41–C44), ν(C29–C41)	1051	ν(C3–C4)	1059	ν(C29–C41)
94	1048 sh	1047 sh	1048	ν(C6–C26)	1047	ν(C26–C32)	1053	ν(C3–C4)
95	1044 m	1041 m	1044	ν(C3–C4)	1042	ν(C29–C41)	1047	ν(C2–C3)
96	1035 m	1028 sh	1027	ρCH_2(C55)	1025	ρCH_2(C55), $\rho' CH_3$(C50)	1027	$\rho' CH_3$(C14)
97	1021 m	1022 m	1026	$\rho' CH_3$(C14)	1023	$\rho' CH_3$(C14)	1024	$\rho' CH_3$(C18)
98		999 s	1021	ν(C31–C35)	1015	ν(C41–C44)	1012	ν(C41–C44)
99	990 s		1005	ν(C41–C44)	1005	ν(C31–C35)	1002	ρCH_2(C55), ν(C47–C50)
100	988 sh		988	ν(C26–C32)	996	$\rho' CH_3$(C35)	994	ν(C26–C32), $\rho' CH_3$(C35)
101			984	$\rho' CH_3$(C35)	984	ν(C26–C32)	986	ν(C26–C32)
102		975 m	969	τwCH_2(C55)	970	τwCH_2(C55)	976	τwCH_2(C55)
103	971 sh		959	ν(C5–C29)	958	ν(C41–C44)	959	ρCH_3(C22)
104	961 w	959 m	957	ρCH_3(C22)	957	ν(C5–C29)	953	ν(C31–O39)
105	951 w	944 sh	954	ρCH_3(C18)	950	ν(C4–C5)	948	ρCH_3(C18)
106	939 s		939	$wagCH_2$(C55)	941	$wagCH_2$(C55), ν(C47–O48)	938	$wagCH_2$(C55)
107	939 s		933	ρCH_3(C35)	936	$wagCH_2$(C55)	934	τwCH_2(C3)
108	923 sh	922 s	927	ν(C31–O39)	928	τwCH_2(C3)	923	ν(C1–C18)
109	917 vs		924	ν(C1–C18)	922	ν(C1–C18), $\rho' CH_3$(C18)	918	ν(C31–O39), ρCH_3(C35)
110	917 vs		918	ν(C47–O48)	913	ν(C31–O39)	913	ν(C47–O48)
111	912 sh		906	ν(C47–C54)	897	ν(C31–O39)	899	$\rho' CH_3$(C50)
112	898 m	900 m	898	ν(C1–C2)	890	ρCH_3(C50)	886	ν(C5–C29), ν(C4–C5)
113	883 w	887 s	879	τwCH_2(C26)	879	τwCH_2(C26)	878	τwCH_2(C26)
114	860 w	858 w	859	ν(C2–C3)	872	τwCH_2(C41)	857	ν(C1–C14)
115	846 w	850 w	851	ν(C5–C22)	851	ν(C2–C3)	846	ν(C47–C54)
116	835 w	826 w	827	τwCH_2(C41), τwCH_2(C44)	833	ν(C5–C22)	840	τwCH_2(C41)
117	817 w	785 sh	797	τwCH_2(C4), τwCH_2(C2)	796	τwCH_2(C4), τwCH_2(C2)	796	τwCH_2(C2), τwCH_2(C4)
118	777 sh	771 s	777	τwCH_2(C32)	776	τwCH_2(C32)	774	τwCH_2(C32)
119	756 m	756 m	769	τwCH_2(C3), ν(C5–C6)	766	τwCH_2(C44)	767	τwCH_2(C44)
120	727 w	733 vs	746	δC41C29C31	739	ν(C1–C2), ν(C1–C14)	738	ν(C5–C6)
121	690 m	709 sh	731	ν(C1–C14)	725	ν(C47–C50), ν(C47–C54)	708	ν(C31–C35)
122	690 m	709 sh	709	ν(C41–C44)	708	ν(C5–C6)	703	ν(C5–C22)
123		686 vw	691	ν(C41–C44)	679	τwCH_2(C41), ν(C29–C31)	680	γ(C55–C54
124	669 w		662	γ(C55–C54)	675	γ(C55–C54)	654	ν(C29–C31)
125		642 vw	635	ν(C6–C1)	641	τO48H49	645	δC41C29C5, ν(C6–C1)
126		573 s	593	τO39H40	624	τO48H49	567	τO39H40
127			578	ρC47O48	587	ρC47O48	559	ρC47O48
128		547 s	548	βR_1(A1)	550	βR_1(A2)	553	τO39H40, ρC47O48
129		517 m	545	βR_1(A2)	542	βR_1(A1)	536	βR_1(A1), τwCH_2(C3)
130		506 sh	538	ρC5C22	533	δC41C29C31, δC35C31C29	524	βR_1(A2)
131			501	βR_2(A1)	499	βR_2(A1)	507	βR_1(A1)
132		481 s	484	βR_3(A2), ρ′C31O39	479	βR_3(A2)	484	ρ′C47O48
133			472	$wagCC_2$(C1), βR_2(A2)	474	βR_2(A2)	476	ρC31O39, $wagCC_2$(C1)
134		447 vw	459	δC41C44C47	470	ρ′C47O48	465	ρ′C31O39, βR_2(A2)
135		430 vw	440	βR_3(A1)	448	δC29C41C44	440	βR_3(A1)
136			431	ρ′C47O48	439	βR_3(A1)	424	δC54C47C44
137		407 sh	423	τR_1(A1)	415	δC14C1C18, δC35C31C32	417	τR_1(A1)
138		391 m	394	δC35C31C32	407	δC35C31C32, $wagCC_2$(C1)	409	δC29C41C44
139		363 m	381	δC41C29C5	378	τwCC_2(C1)	392	δC35C31C32
140			378	τO48H49	368	τwCC_2(C1), ρC47O48	372	τwCC_2(C1)
141		339 sh	374	τwCC_2(C1)	353	τO39H40	348	βR_2(A1), δC50C47C54
142			347	τR_1(A2)	349	ρC31O39	344	δC14C1C18
143		329 m	344	δC14C1C18, δC50C47C44	343	δC14C1C18, δC50C47C44	337	δC41C29C31
144			339	δC50C47C44	333	ρ′C5C22	327	ρ′C5C22
145			328	ρC31O39	325	δC50C47C44	322	ρC5C22
146		309 w	317	ρC5C22, ρCC_2(C1)	318	δC14C1C18	315	ρCC_2(C1), τR_1(A2)
147			315	δC14C1C18	315	τO39H40, ρ′C5C22	308	δC47C54C55

Table 1 (*continued*)

Modes	Experimental		C1		C2		C3	
	IR[a]	Raman[a]	SQM[b]	Assignment[a]	SQM[b]	Assignment[a]	SQM[b]	Assignment[a]
148		286 m	311	δC47C54C55	307	ρCC_2(C1)	297	ρCC_2(C1)
149			306	δC50C47C54	298	δC47C54C55, δC50C47C54	286	δC35C31C29
150		272 sh	292	ρCC_2(C1)	285	ρ′C31O39	277	τO48H49
151		269 w	270	δC35C31C29, ρ′C5C22	270	τR_3(A1)	267	τR_3(A1)
152			268	τR_3(A1)	250	δC26C6C1	249	τR_1(A2)
153		239 s	253	τwCH_3(C18)	241	τwCH_3(C18)	244	δC41C29C5, δC4C5C29
154			244	δC4C5C29	236	τwCH_3(C22), ρC5C22, δC4C5C29	240	τwCH_3(C18)
155			237	τwCH_3(C50)	225	τwCH_3(C50)	236	τwCH_3(C50)
156		213 w	220	τwCH_3(C14)	223	τwCH_3(C14)	224	δC50C47C44
157		204 w	217	τwCH_3(C14), τwCH_3(C18)	203	δC54C47C44	215	βR_3(A2)
158		188 w	204	δC54C47C44	192	τwCH_3(C14), τwCH_3(C22)	197	τwCH_3(C14)
159		174 sh	184	τwCH_3(C35)	184	τR_1(A2), τR_3(A2)	182	δC41C44C47
160		152 sh	180	τwCH_3(C22)	176	τwCH_3(C35)	171	τwCH_3(C35)
161		141 s	154	τR_2(A1)	149	δC41C44C47, δC41C29C5	161	τwCH_3(C22)
162			141	τwC47–C44	133	τR_2(A1)	124	τR_2(A1)
163			127	τR_2(A2)	114	τC47–C54	114	τR_3(A2)
164			102	τC47–C54	110	τwC47–C44	97	τC47–C54
165			86	τR_2(A2), τC47–C54	77	τR_2(A2)	87	τR_2(A2)
166				τwC47–C44[c]		τC47–C54[c]	56	τwC47–C44
167			62	τR_3(A2)	45	τwC47–C44	36	τC41–C29
168			49	τC41–C29	40	τC41–C29	1	τC41–C29, τR_2(A2)

[a] This work.
[b] From scaled quantum mechanics force field.
[c] Assigned by *GaussView* program [32].

and in accordance with similar compounds [10,11,44,45,48,49,56], as indicated in Table 1.

CH_3 modes. The three configurations of EPI have five CH_3 groups, and all the corresponding vibration modes were easily assigned taking into account the higher PED contribution and the assignments reported for compounds containing this group [10,11,34,36,36–39,44,45,48,49,56]. Thus, the band and the shoulder at 2923 and 2901 cm^{-1}, respectively, in the IR spectrum and the Raman bands between 3051 and 2902 cm^{-1} were assigned to CH_3 stretching modes. The CH_3 deformation modes were assigned to the IR and Raman bands located between 1491 and 1363 cm^{-1}, whereas the corresponding rocking modes were assigned between 1219 and 959 cm^{-1}, as observed in Table 1. The twisting modes were assigned to the region predicted by the calculations and in accordance with similar compounds [10,11,34,36–39,44,45,48,49,56].

CH_2 modes. The three configurations of EPI have eight CH_2 groups, seven of which correspond to C atoms in sp^2 hybridization. The remaining group corresponds to the —HC═CH_2 group. The assignments corresponding to the expected vibration modes were performed in accordance with the SQM calculations and to the assignments for similar compounds [10,11,34,36–39,44,45,48,49,56], as described in Table 1.

Skeletal modes. In the three C1, C2 and C3 configurations of EPI, only a C═C stretching mode belonging to the HC═CH_2 group is expected in each configuration in the 1660–1656 cm^{-1} region, as predicted by the SQM calculations. These modes were easily assigned to the IR and Raman bands at 1653 and 1651 cm^{-1}, respectively. The remaining C—C stretching modes are predicted between 1406 and 679 cm^{-1} an were thus assigned to the IR and Raman bands located between 1411 and 686 cm^{-1}, as can be observed in Table 1. The SQM calculations clearly predicted the two C═O stretching modes belonging to the CO═H group; hence, they were assigned to the strong IR bands at 1156, 939 and 917 cm^{-1} and to the Raman band of medium intensity at 1177 cm^{-1}. The remaining skeletal modes were assigned as observed in Table 1.

Force field

As described in Section 'Computational details', the SQM methodology [19] and the MolVib program [33] were employed to calculate the force constants at the B3LYP/6-31G* approximation level from the corresponding scaled force fields expressed in internal coordinates. Table 2 shows the force constants values for the three configurations of EPI, which were compared with those reported for other sesquiterpenoids, such as dehydrofukinone and cnicin [10,11]. The lower value of *f*(νOH) for C1, in relation to C3, can be justified by the corresponding average value of the involved distance because this variable has a value of 0.975 Å in C1, which is slightly higher than the corresponding values found for C3 (0.971 Å), whereas the higher value of the force constant in cnicin is justified by the presence of three OH groups [11]. The slightly lower values of the *f*(νC═C) and *f*(νCH_2)sp^3 force constants found for the three configurations of EPI, in relation to those corresponding to cnicin, could be related to the presence of only a C═C bond in each configuration of EPI, whereas the presence of four C═C bonds in cnicin could justify such differences. On the contrary, the slightly

Table 2
Comparison of scaled internal force constants for 13-*epi*-sclareol.

Force constant	B3LYP/6–31G*[a]				
	C1	C2	C3	Cnicin[b]	Dehydrofukinone[c]
f(νO—H)	6.92	6.87	7.01	6.99	
f(νC—O)	4.47	4.48	4.45	5.44	
f(νC═C)	9.13	9.18	9.13	9.20	8.46
f(νCH_2)sp^3	4.74	4.76	4.76	4.79	4.76
f(νCH_2)sp^2	5.20	5.20	5.20	5.22	
f(νCH_3)	4.91	4.91	4.89	4.18	4.87
f(δCH_2)sp^3	0.76	0.76	0.76	0.76	0.73
f(δCH_2)sp^2	0.43	0.43	0.43	0.44	
f(δCH_3)	0.56	0.56	0.56	0.56	0.55

Units are mdyn $Å^{-1}$ for stretching and stretching/stretching interaction and mdyn Å rad^{-2} for angle deformations.
[a] This work.
[b] From Ref [11].
[c] From Ref [10].

Table 3
TD-DFT calculated visible absorption wavelengths (nm) and oscillator strengths (*f*) for 13-*epi*-sclareol.

B3LYP6-31G*[a]									Experimental[a]	
C1			C2			C3			Exp.[a] λ (nm)	Assignment[a]
Energy transition[a] (eV)	λ (nm)	*f*	Energy transition[a] (eV)	λ (nm)	*f*	Energy transition[a] (eV)	λ (nm)	*f*		
5.7721	214.80	0.0015	6.5281	189.92[c]	0.0950	5.9405	208.71	0.0004		$\pi \rightarrow \pi^*$ (C=C)
6.0657	204.40	0.0002	7.3393	168.93	0.0347	6.8386	181.30	0.0109		$n \rightarrow \sigma^*$
6.1611	201.24[b]	0.0252	7.3719	168.18	0.0373	6.9401	178.65	0.0098	215	$n \rightarrow \sigma^*$
6.2992	196.83	0.0026	7.5181	164.91	0.0292	7.0435	176.03	0.0031		$n \rightarrow \sigma^*$
6.3337	195.75	0.0024	7.6278	162.54[b]	0.2335	7.1268	173.97[b]	0.0123		$n \rightarrow \sigma^*$

[a] This work.
[b] Position maximum.
[c] Shoulder.

higher value observed for the $f(\nu CH_2)sp^3$ force constant in cnicin cannot be justified by the number of CH_2 groups because each configuration of EPI has eight groups, whereas cnicin only has five [11]. These differences are caused by the presence of CH_2 groups in two fused rings (one planar with five members and the other with ten members) that adopt a chair configuration. On the other hand, the slightly higher values of the $f(\nu CH_3)$ force constants for the three configurations of EPI, in relation to cnicin, could be associated with the presence of five CH_3 groups in EPI, whereas there is only one CH_3 group in cnicin. Thus, the similar value of 4.87 mdyn $Å^{-1}$ in dehydrofukinone is justified due to its four CH_3 groups. In general, the calculated values for the $f(\nu CH_2)sp^2$, $f(\delta CH_2)sp^3$, $f(\delta CH_2)sp^2$, and $f(\delta CH_3)$ force constants do not present variations with the structural modifications among C1, C2, C3 and cnicin, and moreover, the values are in accordance with those values reported for molecules containing similar groups [10,11,34,36–39,44,45,48,49,56].

Ultraviolet–Visible spectrum

Fig. S8 shows a comparison of the calculated electronic spectra for the three configurations of EPI at the B3LYP/6-31G* approximation level with the corresponding experimental of the compound in ethanol 96°. Table 3 summarizes all the bands calculated for the three configurations of EPI. The experimental spectrum shows an intense band located at 215 nm, which should be assigned to the chromophores present in the molecule, >C=C< and OH groups. In dehydrofukinone, the band at 208 nm was assigned to the $\pi \rightarrow \pi^*$ transition corresponding to the C=C chromophore [10]; in this case, the broad band centered at 215 nm can be assigned to that transition. To the C2 configuration, the theoretical calculations predict an intense band and a shoulder located in different positions while for the C1 and C3 configurations, only one band is predicted by calculations, as observed in Table 3. Here, the OH groups could act as auxochromes, which probably increase the intensity of the band observed in the experimental spectrum. Note that C1 is in good agreement with the experimental result, however, for C2 (165.54 nm) and C3 (173.97 nm) there is a far discrepancy in theoretical results compared to the experimental (215 nm). The differences in the position of the maxima for C2 and C3 can be explained of two forms. In a first case, the theoretical calculations predicted for the three conformers electronic $\Delta ET_{LP\rightarrow\sigma*}$ transitions, from non-bonding orbitals to sigma anti-bonding orbitals ($_{n\rightarrow\sigma*}$, Table S8). Thus, the differences between the maximum values for C1 and C2 (215.00–165.64 nm = 50 nm) is 0.13 eV and between C1 and C3 is 0.10 eV (315.00–173.97 nm = 41.03 nm) both can be easily explained taking into account the energy values between the $\Delta ET_{LP\rightarrow\sigma*}$ transitions for C1 and C2 (133.05–122.02 = 11.03 kJ/mol = 0.11 eV) and for C1 and C3 (122.02–120.27 = 1.7 kJ/mol = 0.018 eV), as observed in Table S8. Thus, the shifting of the maximum is higher for C2. In a second case, it has possible justified the differences taking into account that the visible absorption maxima of EPI correspond to the electron transition between frontier orbitals such as translation from HOMO to LUMO. Thus, the gap value (HOMO–LUMO) for C1 is 6.83 eV, for C2 is 7.57 eV and, for C3 is 6.55 eV. The difference between C1 and C2 is 0.74 eV while between C1 and C3 is 0.28 eV. Hence, we observed that the shifting of the maximum is bigger for C2 in relation to C3. Both cases justify a higher shifting for C2 in relation to C3.

Conclusions

13-*epi*-sclareol was isolated from *I. tschudiana* Fenzl and characterized by IR, Raman, UV–Vis and NMR spectroscopic techniques in the liquid state. Three stable minimum energy structures for the compound were found in PES, and these were optimized using the hybrid B3LYP/6-31G* method. The two six-membered rings of each configuration adopt chair conformations. The low energy difference between C1 and C2 and between C1 and C3 shows that the three forms could be present in the liquid state. The structural properties for the three configurations, such as their molecular electrostatic potentials, atomic charges, bond orders, stabilization energies and topological properties were computed at the same approximation level. The different O---H and H---H interactions for the three configurations of 13-*epi*-sclareol were studied by NBO and AIM calculations. The first study showed that C1 and C3 have higher stabilities than C2, suggesting their presence in the liquid state, whereas the AIM analysis showed the strong dependence of the interactions on the distance between the involved atoms. The SQM force fields for the three configurations using the B3LYP/6-31G* theory level were presented with the scaled force constants values; a complete assignment of the 168 normal vibration modes for the three structures of the compound was performed. Good concordances were found between the theoretical and experimental UV–Vis and NMR spectra.

Acknowledgements

This work was supported with grants from CIUNT (Consejo de Investigaciones, Universidad Nacional de Tucumán) and CONICET (Consejo Nacional de Investigaciones Científicas y Técnicas, R. Argentina). The authors thank Prof. Tom Sundius for his permission to use MolVib.

Appendix A. Supplementary material

Supplementary data associated with this article can be found, in the online version, at http://dx.doi.org/10.1016/j.saa.2014.11.049.

References

[1] G. Nowak, M. Holub, M. Budesinsky, Acta Soc. Bot. Pol. 58 (1989) 95.
[2] L.P. Christensen, J. Lam, Phytochemistry 29 (1990) 2753.
[3] L.P. Christensen, J. Lam, Phytochemistry 30 (1991) 3289.
[4] I. Landau, H. Mueller-Scharer, P.I. Ward, J. Chem. Ecol. 20 (1994) 929–942.
[5] A. Steinbach, A.J. Scheidig, C.D. Klein, J. Med. Chem. 51 (16) (2008) 5143–5147.
[6] A.M. Fortuna, E.C. Riscala, C.A.N. Catalán, T.E. Gedris, w. Herz, Biochem. Systematyics Ecol. 29 (2001) 967–971.
[7] A.M. Fortuna, E.C. Riscala, C.A.N. Catalán, T.E. Gedris, W. Herz, Biochem. Systematyics Ecol. 30 (2002) 805–808.
[8] M.E. Sesto Cabral, A.M. Fortuna, E.C. Riscala, C.A.N. Catalán, E.E. Sigtad, Allelopathy J. 21 (2008) 175–183.
[9] K.J. öhrer, M. Obkircher, D. Neureiter, J. Parteli, C. Zelle-Rieser, E. Maizner, J. Kern, M. Hermann, F. Hamacher, O. Merkel, N. Wacht, C. Zidorn, M. Scheideler, R. Greil, J. Mol. Med. 90 (6) (2012) 681–693.
[10] E. Lizarraga, E. Romano, A.B. Raschi, P. Leyton, C. Paipa, S.A. Brandán, A.C.N. Catalán, J. Mol. Struct. 1048 (2013) 331–338.
[11] F. Chain, E. Romano, P. Leyton, C. Paipa, C.A.N. Catalán, M.A. Fortuna, S.A. Brandán, J. Mol. Struct. 1065–1066 (2014) 160–169.
[12] Z. Guo, G.J. Wagner, Planta 197 (1995) 627–632.
[13] J.A. Bailey, G.G. Vincent, R.S. Burden, J. Gen. Microbiol. 85 (1974) 57–64.
[14] L. Mendoza, L. Tapia, M. Wilkens, A. Urzua, Bol. Soc. Chil. Quím. 47 (2002) 091–098.
[15] L. Tapia, J. Torres, L. Mendoza, A. Urzúa, J. Ferreira, M. Pavani, M. Wilkens, Planta Med. 70 (11) (2004) 1058–1063.
[16] K.V. Sashidhara, J.N. Rosaiah, A. Kumar, H.K. Bid, R. Konwar, N. Chattopadhyay, Phytother Res. 21 (11) (2007) 1105–1108.
[17] A. Urzúa, M.C. Rezende, C. Mascayano, L. Vásquez, Molecules 13 (2008) 882–891.
[18] G. Bernardinelli, C. Vial, S. Starkemann, F. Näf, Acta Cryst. C44 (1988) 715–717.
[19] (a) G. Rauhut, P. Pulay, J. Phys. Chem. 99 (1995) 3093–3100;
(b) G. Rauhut, P. Pulay, J. Phys. Chem. 99 (1995) 14572.
[20] B.H. Besler, K.M. Merz Jr., P.A. Kollman, J. Comp. Chem. 11 (1990) 431–439.
[21] A.E. Reed, L.A. Curtis, F. Weinhold, Chem. Rev. 88 (6) (1988) 899–926.
[22] E.D. Glendening, J.K. Badenhoop, A.D. Reed, J.E. Carpenter, F. Weinhold, NBO 3.1, Theoretical Chemistry Institute, University of Wisconsin, Madison, WI, 1996.
[23] R.F.W. Bader, Atoms in Molecules, A Quantum Theory, Oxford University Press, Oxford, 1990. ISBN: 0198558651.
[24] F. Biegler-Köning, J. Schönbohm, D. Bayles, AIM2000, J. Comput. Chem. 22 (2001) 545–559.
[25] R.G. Parr, R.G. Pearson, J. Am. Chem. Soc. 105 (1983) 7512–7516.
[26] S. Turbay, O. Piro, G. Echeverría, A. Navarro, M. Fernandez-Liencres, M. Fortuna, M. Tuttolomondo, Spectrochim. Acta Part A 123 (2014) 71–77.
[27] S.C. Demetzo, C. Harvala, S.M. Phillianos, J. Nat. Prod. 53 (1990) 1365–1368.
[28] D.B. Stierle, A.A. Stierle, R.D. Larsen, Phytochemistry 27 (2) (1988) 517–522.
[29] A.B. Nielsen, A.J. Holder, Gauss View 5.0, User's Reference, GAUSSIAN Inc., Pittsburgh, PA, 2009.
[30] A.D. Becke, J. Chem. Phys. 98 (1993) 5648–5652.
[31] C. Lee, W. Yang, R.G. Parr, Phys. Rev. B 37 (1988) 785–789.
[32] M.J. Frisch, G.W. Trucks, H.B. Schlegel, G.E. Scuseria, M.A. Robb, J.R. Cheeseman, J.A. Montgomery Jr., T. Vreven, K.N. Kudin, J.C. Burant, J.M. Millam, S.S. Iyengar, J. Tomasi, V. Barone, B. Mennucci, M. Cossi, G. Scalmani, N. Rega, G.A. Petersson, H. Nakatsuji, M. Hada, M. Ehara, K. Toyota, R. Fukuda, J. Hasegawa, M. Ishida, T. Nakajima, Y. Honda, O. Kitao, H. Nakai, M. Klene, X. Li, J.E. Knox, H.P. Hratchian, J.B. Cross, C. Adamo, J. Jaramillo, R. Gomperts, R.E. Stratmann, O. Yazyev, A.J. Austin, R. Cammi, C. Pomelli, J.W. Ochterski, P.Y. Ayala, K. Morokuma, G.A. Voth, P. Salvador, J.J. Dannenberg, V.G. Zakrzewski, S. Dapprich, A.D. Daniels, M.C. Strain, O. Farkas, D.K. Malick, A.D. Rabuck, K. Raghavachari, J.B. Foresman, J.V. Ortiz, Q. Cui, A.G. Baboul, S. Clifford, J. Cioslowski, B.B. Stefanov, G. Liu, A. Liashenko, P. Piskorz, I. Komaromi, R.L. Martin, D.J. Fox, T. Keith, M.A. Al-Laham, C.Y. Peng, A. Nanayakkara, M. Challacombe, P.M.W. Gill, B. Johnson, W. Chen, M.W. Wong, C. Gonzalez, J.A. Pople, Gaussian 09, Revision A.02, Gaussian, Inc.: Pittsburgh, PA, 2009.
[33] T. Sundius, Vib. Spectrosc. 29 (2002) 89–95.
[34] G.R. Argañaraz, E. Romano, J. Zinczuk, S.A. Brandán, J. Chem. Chem. Eng. 5 (2011) 747–758.
[35] C.D. Contreras, M. Montejo, J.J. Lopez Gonzalez, J. Zinczuk, S.A. Brandán, J. Raman Spectrosc. 42 (1) (2011) 108–116.
[36] E. Romano, A.B. Raschi, A. Benavente, S.A. Brandán, Spectrochim. Acta, Part A 84 (2011) 111–116.
[37] E. Romano, M.V. Castillo, J.L. Pergomet, J. Zinczuk, S.A. Brandán, J. Mol. Struct. 1018 (2012) 149–155.
[38] P. Leyton, J. Brunet, V. Silva, C. Paipa, M.V. Castillo, S.A. Brandán, Spectrochim. Acta, Part A 88 (2012) 162–170.
[39] S.A. Brandán, F. Marquez Lopez, M. Montejo, J.J. Lopez Gonzalez, A. Ben Altabef, Spectrochim. Acta, Part A 75 (2010) 1422–1434.
[40] E. Romano, N.A.J. Soria, R. Rudyk, S.A. Brandán, Mol. Simul. 38 (7) (2012) 561–566.
[41] A. Brizuela, E. Romano, A. Yurquina, S. Locatelli, S.A. Brandán, Spectrochim. Acta Part A 95 (2012) 399–406.
[42] P. Leyton, C. Paipa, A. Berrios, A. Zárate, S. Fuentes, M.V. Castillo, S.A. Brandán, J. Mol. Struct. 1031 (2013) 110–118.
[43] M.V. Castillo, E. Romano, A.B. Raschi, A. Yurquina, S.A. Brandán, Comput. Theor. Chem. 995 (2012) 43–48.
[44] E. Lizarraga, E. Romano, R.A. Rudyk, C.A.N. Catalán, S.A. Brandán, Spectrochim. Acta Part A 97 (2012) 202–208.
[45] E. Lizarraga, E. Romano, A.B. Raschi, P. Leyton, C. Paipa, C.A.N. Catalán, S.A. Brandán, J. Mol. Struct. 1048 (2013) 331–338.
[46] E. Romano, M.F. Ladetto, S.A. Brandán, Comput. Theor. Chem. 1011 (2013) 57–64.
[47] R. Ditchfield, Mol. Phys. 8 (1974) 397–409.
[48] O.E. Piro, G.A. Echeverría, E. Lizárraga, E. Romano, C.A.N. Catalán, S.A. Brandán, Spectrochim. Acta Part A 101 (2013) 196–203.
[49] E. Romano, J.L. Pergomet, J. Zinczuk, S.A. Brandán, Structural and vibrational properties of some quinoline acetic acid derivatives with potentials biological activities, in: Acetic Acids: Chemical Properties, Production and Applications, Edited Collection, Nova Science Publishers, 2013.
[50] A.E. Ledesma, S.A. Brandán, J. Zinczuk, O.E. Piro, J. López González, A. Ben Altabef, J. Phys. Org. Chem. 21 (12) (2008) 1086–1097.
[51] S.A. Brandán, G. Benzal, J.V. García-Ramos, J.C. Otero, A. Ben Altabef, Vib. Spectrosc. 46 (2008) 89–99.
[52] S.A. Brandán, E. Eroğlu, A.E. Ledesma, O. Oltulu, O.B. Yalçınkaya, J. Mol. Struct. 993 (2011) 225–231.
[53] Zhang, Fei, Acta Cryst. E67 (2011) o2957.
[54] M. Paul, A. Radha, D.S. Kumar, J. D. Med. 5 (1) (2013) 69–78.
[55] J-C. Caissard, T. Olivier, C. Delbecque, S. Palle, P.-P. Garry, A. Audran, N. Valot, S. Moja, F. Nicole, J.-L. Magnard, S. Legrand, S. Baudino, F. Jullien, PLoS One 7 (10) (2012) e48253.
[56] A.B. Brizuela, L.C. Bichara, E. Romano, A. Yurquina, S. Locatelli, S.A. Brandán, Carbohydr. Res. 361 (2012) 212–218.